49th AIAA Aerospace Sciences Meeting including the New Horizons Forum and Aerospace Exposition
4 - 7 January 2011, Orlando, Florida
AIAA 2011-376

Nonlinear Structural Response in Flexible Flapping Wings with Different Density Ratio

Min Xu*, Mingjun Wei†, Tao Yang‡, Young S. Lee§, Thomas D. Burton¶
New Mexico State University, Las Cruces, NM 88003

In our previous work, a strong-coupling approach was successfully used to simulate highly flexible wings interacting with surrounding fluid flows in a globally Eulerian framework for both fluid and solid. However there was a strong assumption to simplify the formulation: the wing structure has the same density as the surrounding fluid. Here, using a fast-tracking method to efficiently identify the solid and fluid areas and solving modified momentum equations and pressure Poisson equation with variable (but still incompressible) density, we were able to apply the same idea to solve flapping-wing system with arbitrary density ratio. In the investigation of effects by different density ratio, for the same shear modulus, higher structural density actually leads to a "softer" appearance with larger deformation of the wing, as a result of relatively stronger inertial effect. Meanwhile, the wake structure changes from inverse Kármán vortex street to Kármán vortex street and results in a transition from thrust producing to drag producing. Using Euler-Bernoulli beam theory, we analytically obtained the first three natural frequencies and their corresponding modes for the same wing used in numerical simulation. We found that the basic dynamics can be adequately described by these three modes and the leading frequency. The linear analysis also predicts the appearance of higher modes at larger density ratio in our nonlinear numerical simulations. On the other hand, the structure shows responses at higher frequency, especially for higher modes, as a clear indication of the system's nonlinearity.

I. Introduction

Birds and insects have survived by taking the advantage of flapping flexible wings for high energy efficiency and incredible maneuverability, when fixed-wing design of conventional airplanes fails at the same low Reynolds number. The flapping-wing design from the nature has inspired human being to manufacture those from ancient flight machines to modern unmanned aerial vehicles. Especially, with the recent demand of micro air vehicles (MAVs), flapping-wing design draws its attention by many desirable characteristics at low Reynolds number regime.[1]

Starting with the pioneer work by Knoller[2] and Betz[3] in thrust generation by a flapping wing, numerous research in experiments and numerical simulation has been done to understand the propulsion by flapping wings and was summarized in various places.[4–7] Because of extra complexity brought in by wing flexibility, majority of works focused on rigid wings[4,8–10] or prescribed deformable wings.[11,12] However, recently, there was increasing interest and number of works in truly flexible wings with fully coupled fluid-structure interaction in both experiments and numerical simulation.[7,13–15]

In our study, we used a strong-coupling approach to simulate highly flexible wings interacting with surrounding fluid flows in a globally Eulerian framework for both fluid and solid. The idea was based on an

*PhD Candidate, Department of Mechanical and Aerospace Engineering
†Assistant Professor, Department of Mechanical and Aerospace Engineering, Senior Member AIAA
‡PhD Candidate, Department of Mechanical and Aerospace Engineering, Student Member AIAA
§Assistant Professor, Department of Mechanical and Aerospace Engineering, Member AIAA
¶Professor, Department of Mechanical and Aerospace Engineering, Senior Member AIAA

Copyright © 2011 by Mingjun Wei. Published by the American Institute of Aeronautics and Astronautics, Inc., with permission.

immersed boundary approach solving a combined Eulerian fluid-solid equation proposed by Zhao, Freund, and Moser (ZFM).[16] To control the flapping trajectory, Yang, Wei, and Zhao (YWZ)[15] later modified ZFM algorithm to include control cells. In both ZFM and YWZ formulations, they made the same assumption of using the same density for both solid and fluid. This assumption successfully simplified the algorithm and reduced the computational cost, however, it also made impossible to study the effect from mass ratio which was listed as one of similarity parameters by Ishihara et al.[13] Here, based on YWZ formulation and following the same idea, we extend the algorithm to handle arbitrary mass ratio. A fast-tracking method is introduced to dynamically recognize the solid points on Cartesian mesh. Then, the discontinuity of density is included by modifying the original pressure Poisson equation with a variable mass ratio coefficient and the momentum equation with variable density. The new approach allows us to study the propulsion features and structure responses by wings with different densities. Furthermore, structural analysis based on Euler-Bernoulli beam theory and the mode decomposition of our system were conducted.

For the rest of the paper, the algorithm details are shown in section II, the numerical simulation results and structural analysis are in section III, and the final conclusion is presented in section IV

II. Numerical algorithm

The numerical simulation is based on a monolithic approach to solve fluid motion, solid motion, and their interaction by a combined Eulerian description, while the elastic-stress being solved on a Lagrangian mesh then projected back to the Eulerian mesh as extra bodyforce terms. The original ZFM formulation[16] is

$$\begin{aligned} \nabla \cdot \mathbf{u} &= 0 \\ \frac{\partial \mathbf{u}}{\partial t} + \mathbf{u} \cdot \nabla \mathbf{u} &= -\nabla p + \frac{1}{Re_f} \nabla^2 u + \nabla \cdot \chi_s \boldsymbol{\tau}_{elas}, \end{aligned} \tag{1}$$

where a characteristic function χ_s is defined by

$$\chi_s = \begin{cases} 1 & in \ \ \Omega_s \\ 0 & otherwise \end{cases} \tag{2}$$

to specify solid elasticity in "wing area" Ω_s (figure 1). The fluid Reynolds number is $Re_f = \rho_f^* U^* L^* / \mu_f^*$. A simple nonlinear neo-Hookean model is used for elasticity $\boldsymbol{\tau}_{elas} = \mu_s(\mathbf{A} \cdot \mathbf{A}^T - \mathbf{I})$, where solid shear modulus is nondimensionalized by $\mu_s = \mu_s^* / \rho_s^* (U^*)^2$. However, this formulation lacks the mechanism to define the motion of certain components for desirable moving trajectories (i.e. flapping). Therefore, as shown in figure 1, we implemented rigid control cells inside the elastic body *as skeleton structure to flap the wing.* To assure an accurate description of skeleton's moving trajectory, a typical immersed boundary method using direct-forcing approach[17] was applied on the control cells *only* and fitted into the otherwise elastic body moving passively through fluid-structure interaction (FSI) (figure 2).

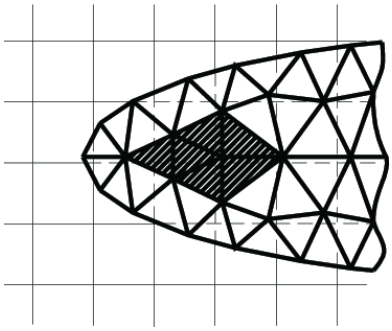

Figure 1. The sketch of mesh configuration for a NACA airfoil: Cartesian mesh with thin lines is the global Eulerian mesh; triangles with thick lines are the local Lagrangian mesh for solid (Ω_s); dark triangles are control cells (Ω_c).

Figure 2. Schematics for flapping motion: control cells are at the leading edge.

Then, the momentum equation with *flapping* capability becomes

$$\frac{\partial \mathbf{u}}{\partial t} + \mathbf{u} \cdot \nabla \mathbf{u} = -\nabla p + \frac{1}{Re_f} \nabla^2 \mathbf{u} + \nabla \cdot \chi_s \boldsymbol{\tau}_{elas} + \chi_c f, \tag{3}$$

where χ_c is defined similarly but with value only in control region Ω_c, and the bodyforce f is applied to prescribe active plunging motion at leading edge. This is exactly the formulation used in YWZ[15] for flapping wing simulation. Both ZFM and YWZ assumed the same density of solid and fluid. To consider the effect from mass ratio $R_\rho = \rho_s/\rho_f$ (the inverse of mass number used by Ishihara et al.[13]), we modify the pressure gradient term with a variable density $\rho_{s,f}$,

$$\frac{\partial \mathbf{u}}{\partial t} + \mathbf{u} \cdot \nabla \mathbf{u} = -\frac{\nabla p}{\rho_{s,f}} + \frac{1}{Re_f} \nabla^2 \mathbf{u} + \nabla \cdot \chi_s \boldsymbol{\tau}_{elas} + \chi_c f, \tag{4}$$

where

$$\rho_{s,f} = \begin{cases} \rho_s & \text{on solid points;} \\ \rho_f & \text{on fluid points.} \end{cases} \tag{5}$$

The solid and fluid densities are non-dimensionalized in a consistent way, such that $\rho_s = \rho_s^*/\rho_f^*$ and $\rho_f = 1$.

In principle, we can use the projection between the global Eulerian mesh and the solid Lagrangian points to trace the solid boundary, in the same way of handing elasticity terms.[15,16] However, the projection between the meshes is expensive, and it becomes less necessary when the value is not sensitive to the locations of solid points. So that, we develop a fast-tracking method to dynamically recognize the location of Eulerian mesh points in fluid or solid areas, and assign the right density accordingly. The method simply goes through all solid cells, where possible Cartesian mesh points are checked if they are inside the cell. The criterion is based on a basic geometric property that a point $\mathbf{P}$ locates inside a triangle $\Delta\mathbf{ABC}$ if $m, n \in [0, 1]$ for m and n being the solution of

$$\mathbf{P} = \mathbf{A} + m(\mathbf{B} - \mathbf{A}) + n(\mathbf{C} - \mathbf{A}), \tag{6}$$

where the symbol of points are referred to their individual Cartesian coordinates. Since the number of solid points is, at least, two orders lower than the total Eulerian mesh points, and the possible Cartesian points reside only in a small box area at the size of a solid cell, the computational cost for this tracking process becomes negligible. With the tracking, all Eulerian points will be assigned solid or fluid densities accordingly for the modified momentum and pressure Poisson equations. It is noticed that the elastic-stress can be distributed to boundary points even geometrically in "fluid" region,[16] the density of these boundary points should be considered as solid for density in order to satisfy the pressure boundary condition.

With the standard projection method for solving incompressible Navier-Stokes equations,[18] the different density between the fluid and solid also ends up with a modified pressure Poisson equation with variable density,

$$\nabla \cdot \frac{\nabla p}{\rho_{s,f}} = \nabla \cdot \hat{\mathbf{u}}, \tag{7}$$

where $\hat{\mathbf{u}}$ is the intermedia velocity for projection method. The equation is ill-conditioned and was solved by Preconditioned Conjugate Gradient Method.

For overall time advancement, we used the same third-order Runge-Kutta/Crank-Nicolson Scheme with direct forcing implemented as being detailed in YWZ.[15] Other numerical details, including the projection/interpolation procedure, are referred to the ZFM work.[16]

III. Simulation results and analysis

The numerical simulation was taken in a square area with $-2 < x < 2$ and $-2 < y < 2$ nondimensionalized by an arbitrary length scale L, which is twice as long as the cord length c of our flexible wings before deformation. A uniform 800×800 Cartesian mesh was used for Eulerian description, while triangular cells were used for Lagrangian description of the wing structure. As shown in figure 2, control cells at the leading edge moved at speed

$$v_x = 0, \qquad v_y = 2ak\pi \cos 2k\pi t, \tag{8}$$

where a is the amplitude of oscillatory motion and k is the frequency. For all cases, we chose $k = 1$ and $a = 0.1$ and studied the effects from mass ratio only. Reynolds number was 500, which is based on the undeformed cord length c, incoming free-stream speed, and fluid properties. The nondimensional solid elastic shear modulus was $\mu_s = 100$. In this section, we first check the flow field and structural deformation, then perform analytical analysis and mode decomposition.

III.A. Wake pattern in fluid flow and the effect on thrust/drag

Figure 3 shows different wake structures (top) and structural deformations (bottom) for flapping wings at different mass ratio $R_\rho = 0.2$, 1, and 5. As the mass ratio R_ρ increases, larger deformation is shown as a result of higher inertial effect. Though the shear modulus keeps the same, the structure appears to be "softer" with larger bending by relatively stronger inertial force. The wake structure behind flapping wings also changes from reverse Kármán vortex street to Kármán vortex street.

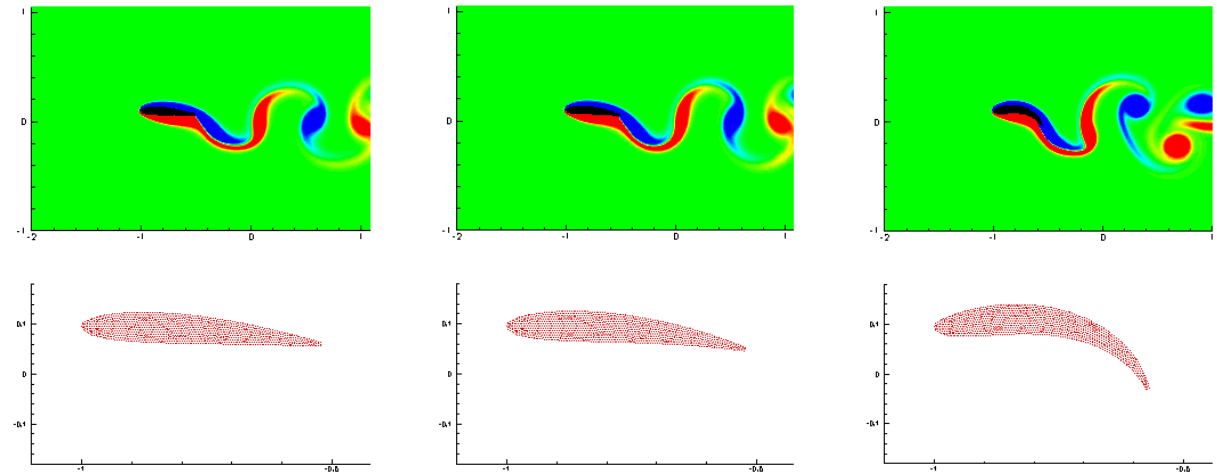

(a) (b) (c)

Figure 3. Wake pattern (top) and zoom-in structure deformation (bottom) of wings flapping at frequency $k = 1$ but with different solid/fluid mass ratio: (a) $R_\rho = 0.2$; (b)$R_\rho = 1$;(c)$R_\rho = 5$.

Figure 4 plots mean velocity profiles at a down stream location $x = 1.0$ for all above cases. The change of mean velocity profile to deficit is a clear indication of the system changing from small thrust producing ($R_\rho = 0.2$ and 1) to actually drag producing ($R_\rho = 5$).

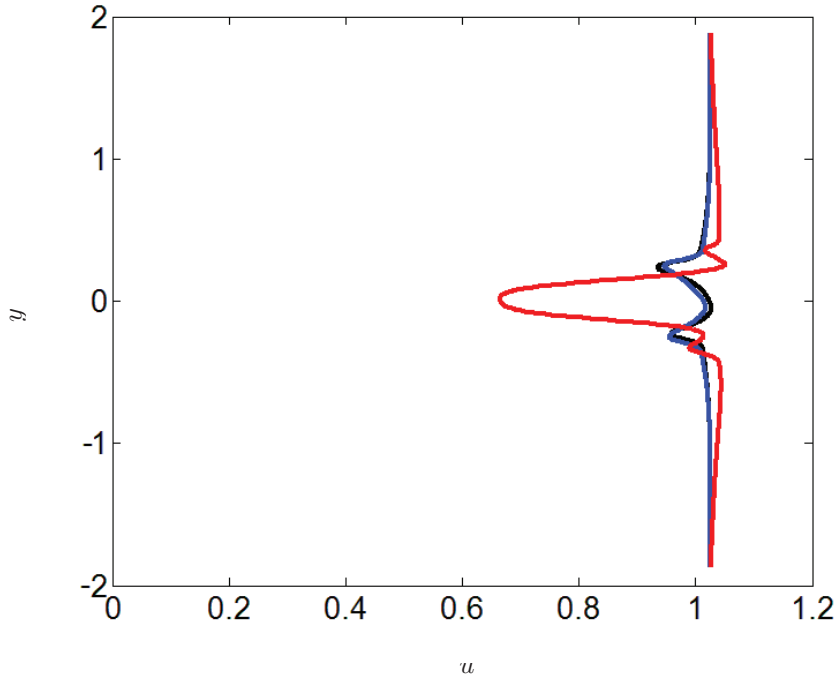

Figure 4. The mean velocity profile at downstream location $x = 1$ for flapping wings with $R_\rho = 0.2$ (———), $R_\rho = 1$ (———), $R_\rho = 5$ (———).

III.B. Structural analysis and mode decomposition

To better understand structural response, we conduct a simple structural analysis using Euler-Bernoulli beam theory.[19] Here, we neglect the coupling between the transverse and axial vibrations and the nonlinearity of constitutive relation (i.e. neo-Hookean relation). The nondimensional equation of motion governing the Euler beam's transverse vibration $y(x,t)$ is

$$R_\rho H(x)\frac{\partial^2 y}{\partial t^2} + \frac{\partial}{\partial x^2}\left[EI(x)\frac{\partial^2 y}{\partial x^2}\right] = P(x,t) \tag{9}$$

with boundary conditions

$$y|_{x=0} = a\sin(2k\pi t), \tag{10}$$

and

$$\left.\frac{\partial y}{\partial x}\right|_{x=0} = \left.\frac{\partial^2 y}{\partial x^2}\right|_{x=l} = \left.\frac{\partial}{\partial x}\left[EI(x)\frac{\partial^2 y}{\partial x^2}\right]\right|_{x=l} = 0, \tag{11}$$

where R_ρ is equivalent to ρ_s by our nondimensionalization, $H(x)$ is the structure thickness, E is Young's modulus ($E = 3\mu_s$ in our case), $I(x)$ is the moment of inertia, l is the length of the beam, $P(x,t)$ is the fluid-structure interaction load. NACA0012 is used in this linear analysis to keep the same configuration as in the nonlinear numerical simulation.

We can separate the leading-edge motion from $y(x,t)$ and set an appropriate $P(x,t)$, so that, (9) changes to a homogeneous problem for the residual $u = y - a\sin(2k\pi t)$ as

$$R_\rho H(x)\frac{\partial^2 u}{\partial t^2} + \frac{\partial}{\partial x^2}\left[EI(x)\frac{\partial^2 u}{\partial x^2}\right] = 0 \tag{12}$$

with boundary conditions

$$u|_{x=0} = \left.\frac{\partial u}{\partial x}\right|_{x=0} = \left.\frac{\partial^2 u}{\partial x^2}\right|_{x=l} = \left.\frac{\partial}{\partial x}\left[EI(x)\frac{\partial^2 u}{\partial x^2}\right]\right|_{x=l} = 0. \tag{13}$$

Using method of variables separation, we can solve (12) as an eigen-value problem and obtain the natural frequency ω_i and natural modes $\Phi_i(x)$ of the NACA0012 beam. It is noticed that the orthonormalization of the natural modes is defined by

$$\int_0^l H(x)\Phi_m(x)\Phi_n(x)dx = \alpha_n\delta_{m,n}, \tag{14}$$

where $\delta_{m,n}$ is Kronecker's delta and α_n is a normalization factor.

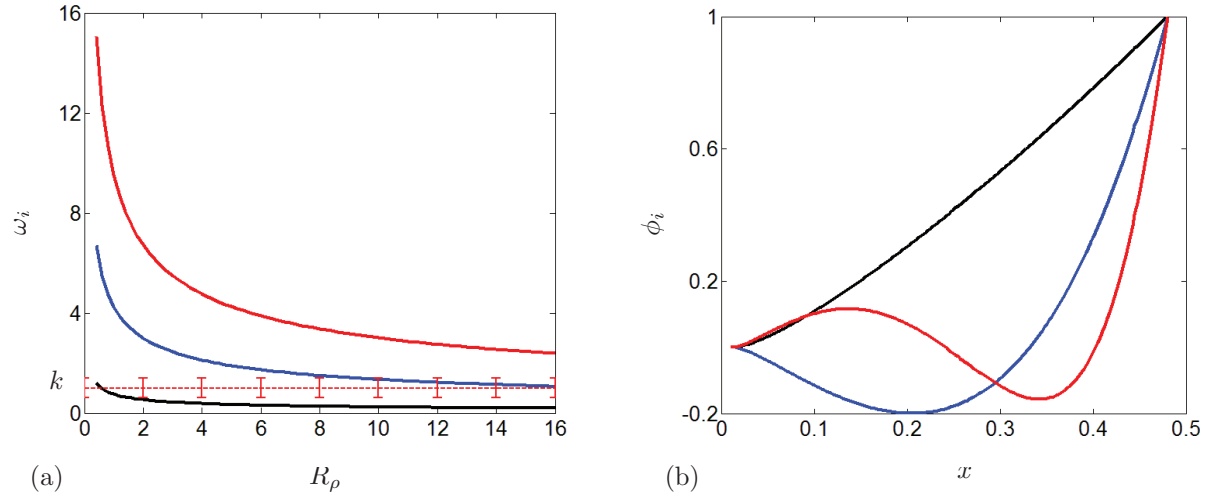

Figure 5. (a)The correlation between mass ratio and the 1st (——), 2nd (——) and 3rd (——) natural frequencies. (b)The 1st (——), 2nd (——) and 3rd (——) natural mode shape.

Figure 5(a) shows the relation between the natural frequencies and mass ratio. The natural frequencies decrease with mass ratio increasing. Therefore, with the same forcing frequency being imposed at the leading edge, it becomes easier to excite higher modes at higher mass ratio. As shown in figure 5(b), the shape of the first mode is almost a straight line, which exists in all cases and can be considered as rigid-body pitching. The higher modes represent different types of bending and contribute to a "softer" appearance at high mass ratio cases. Thus, it is consistent with the observation from numerical simulations.

The solution of (9) can be expanded on the base functions (i.e. natural modes) as

$$y(x,t) = a\sin(2k\pi t) + \sum_{i=1}^{\infty} A_i(t)\Phi_i(x) \tag{15}$$

with the first term for leading-edge plunging motion. We assume that the nonlinear solution from numerical simulation can be approximated by an expansion on the same bases. So, the simulation solution y_{sim}, instead of the linear solution y from (9), can be used to calculate modes' coefficients $A_i(t)$ by using Galerkin projection:

$$A_i(t) = \frac{1}{\alpha_i}\int_0^l [y_{\text{sim}}(x,t) - a\sin(2k\pi t)]H(x)\Phi_i(x)dx \tag{16}$$

Since modes higher than the 3rd order can not be excited, there is no need to include more than three modes in expansion. In fact, figure (6) shows that three modes are adequate to represent the simulation solution.

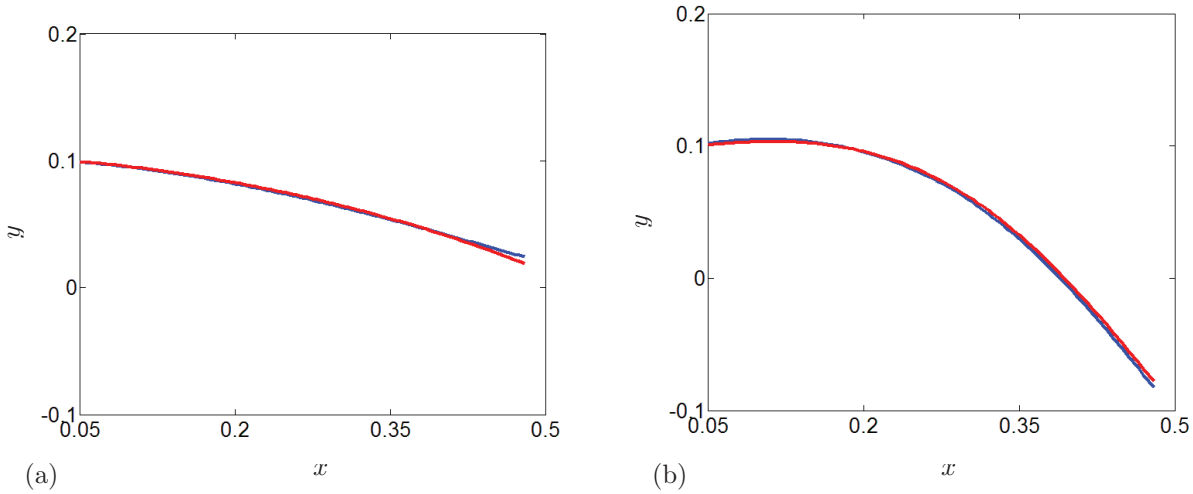

Figure 6. The center line of flapping wing at certain instant obtained from numerical simulation (———) and rebuilt by using three modes (———) at (a)$R_\rho = 0.2$; (b)$R_\rho = 5$.

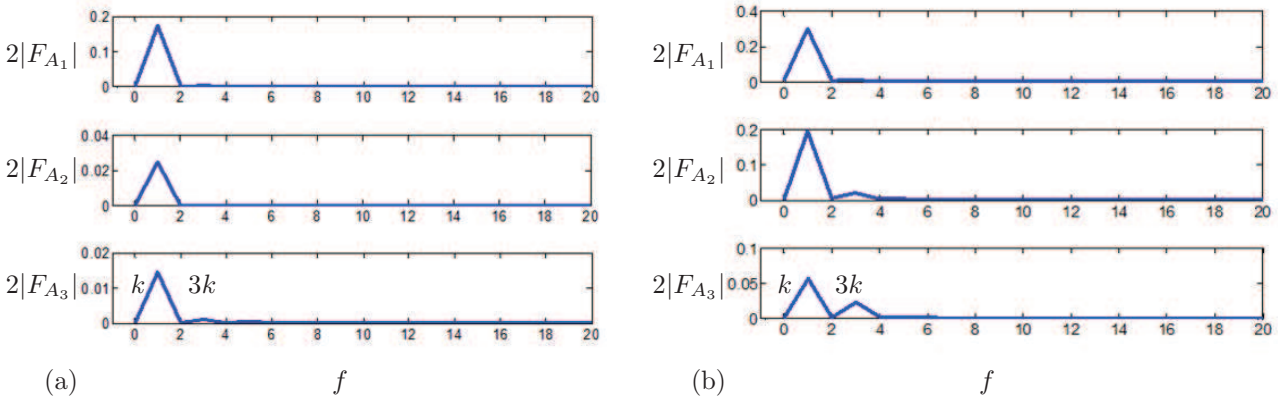

Figure 7. The frequency spectrum of $A_i(t)$ with (a)$R_\rho = 1$; (b)$R_\rho = 10$.

Applying Fourier transform on coefficients $A_i(t)$ yields their frequency spectrum. Two frequencies are observed in figure 7: one is leading-edge forcing frequency k, and the other is $3k$. According to linear vibration theory, the response frequency must be same as excitation frequency. Thus the second frequency can only be introduced by nonlinearity. It is noticed that the amplitude of the second frequency grows with the mass ratio increasing. It is consistent with the increase of nonlinearity when the structure has larger deformation and stronger interaction with the fluid flow.

Overall, the leading-edge forcing frequency still plays a dominant role as shown in figure 7. To further simplify the model, we use only the frequency k to describe the flapping motion as

$$y(x,t) = a\sin(2k\pi t) + \sum_{i=1}^{3} \tilde{A}_{0i}\sin(2k\pi t + \beta_i)\Phi_i(x) \tag{17}$$

where $\tilde{A}_{0i}$ and β_i are the amplitude and phase of each mode with single frequency k.

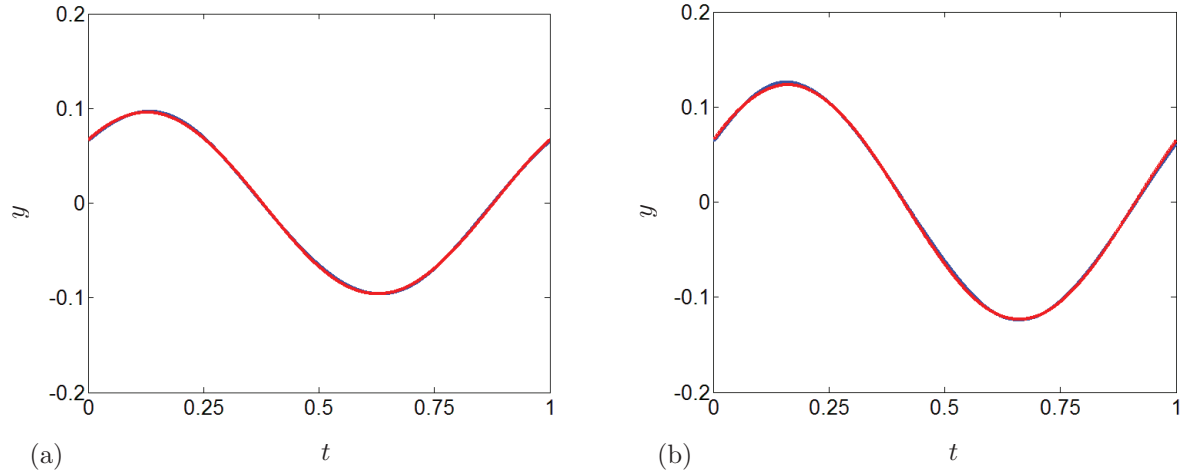

Figure 8. The trajectories of the point at $x = 0.9c$ being obtained from numerical simulation (——) and being rebuilt with three modes at frequency k (——) for (a)$R_\rho = 0.2$; (b)$R_\rho = 5$.

Figure 8 shows that three modes at leading-edge forcing frequency k can approximate the flapping motion well. Thus, the complex nonlinear motion of flexible flapping wing may be approximated well by variables $(\tilde{A}_{0i}, \beta_i)$.

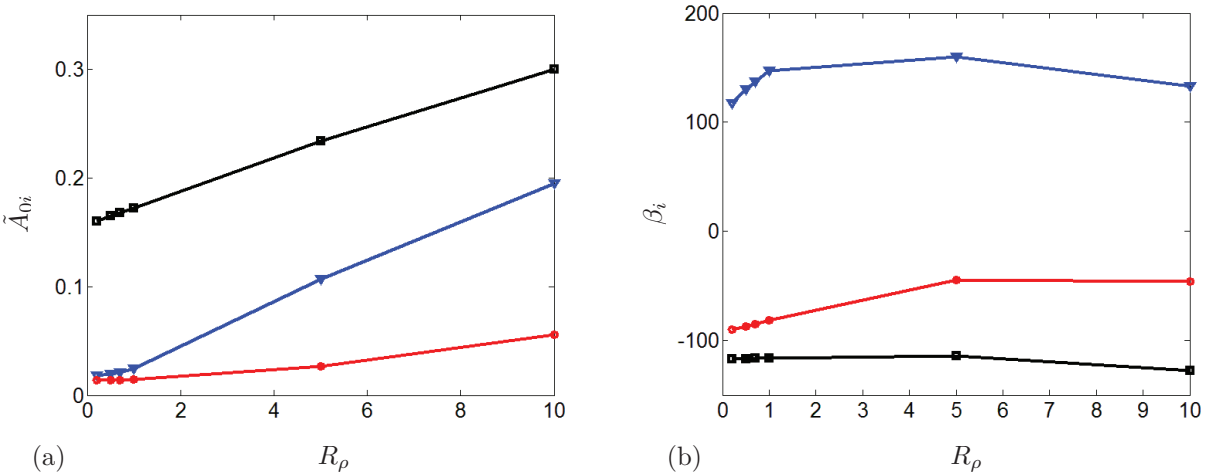

Figure 9. The correlation between mass ratio and (a)amplitude and (b)phase of 1st (——), 2nd (——) and 3rd (——) modes.

Figure 9 shows that the amplitude $\tilde{A}_{0i}$ grows with mass ratio and the high order modes play more important role at higher mass ratio, which is consistent with our previous analysis. The phase of first mode, β_1, keeps about the same at around 90° when the mass ratio changes; while the phase delay of higher modes shows more observable changes which can result in the change of propulsion efficiency.[8]

IV. Conclusion

We have successfully developed a combined algorithm to study the flapping flexible wings with different density for solid and fluid. The overall continuity equation and momentum equations were solved on a uniform Eulerian coordinate, while the solid elasticity and the trajectory of control cells are represent by the body force in corresponding region. The difference in density for solid and fluid is tracked and included in

modified momentum equations and pressure Poisson equation with variable coefficients.

The effect of mass ratio on the propulsion of flapping flexible wings was studied. The structure of wake vortex street and the mean velocity profile at downstream location both show that the flexible wings can turn from thrust producing to drag producing as the mass ratio increasing.

A simple analytical model was set up to study the effect from mass ratio on structural responses. The increase in mass ratio will reduce all natural frequencies. Therefore, natural modes at higher order can be excited easier at higher mass ratio. The higher modes contribute to larger deformation and can be the possible reason for lower propulsion efficiency. Our analysis also shows that the first three modes are adequate in describing current flapping-wing cases and the leading frequency k along contributes to most of the dynamics, though frequency $3k$ starts to appear and play more significant role as the nonlinearity increases.

Acknowledgment

The authors gratefully acknowledge the support from Army Research Lab through Army High Performance Computing Research Center (AHPCRC).

References

[1]Mueller, T. J. and DeLaurier, J. D., "An overview of Micro Air Vehicle aerodynamics," *Fixed and Flapping Wing Aerodynamics for Micro Air Vehicle Applications*, edited by T. J. Mueller, American Institute of Aeronautics and Astronautics, Inc., 2001.

[2]Knoller, R., "Die Gesetze des Luftwiderstandes," *Flug- und Motortechnik (Wien)*, Vol. 3, No. 21, 1909, pp. 1–7.

[3]Betz, A., "Ein Beitrag zur Erklärung des Segelfluges," *Zeitschrift für Flugtechnik and Motorluftschiffahrt*, Vol. 3, 1912, pp. 269–272.

[4]Jones, K. D., Dohring, C. M., and Platzer, M. F., "Experimental and Computational Investigation of the Knoller-Betz Effect," *AIAA J.*, Vol. 36, No. 7, 1998, pp. 1240–1246.

[5]Jones, K. D. and Platzer, M. F., "An experimental and numerical investigation of flapping-wing propulsion," 37th Aerospace Sciences Meeting, Reno, NV, AIAA Paper 99-0995, January 1999.

[6]Jones, K. D. and Platzer, M. F., "Flapping-wing propulsion for a Micro Air Vehicle," 38th Aerospace Sciences Meeting, Reno, NV, AIAA Paper 2000-0897, January 2000.

[7]Heathcote, S. and Gursul, I., "Flexible flapping airfoil propulsion at low Reynolds numbers," *AIAA J.*, Vol. 45, No. 5, 2007, pp. 1066–1079.

[8]Anderson, J. M., Streitlien, K., Barrett, D. S., and Triantafyllou, M. S., "Oscillating foils of high propulsive efficiency," *J. Fluid Mech.*, Vol. 360, 1998, pp. 41–72.

[9]Lai, J. C. S. and Platzer, M. F., "Jet characteristics of a plunging airfoil," *AIAA J.*, Vol. 37, No. 12, 1999, pp. 1529–1537.

[10]Lewin, G. C. and Haj-Hariri, H., "Modelling thrust generation of a two-dimensional heaving airfoil in a viscous flow," *J. Fluid Mech.*, Vol. 492, 2003, pp. 339–362.

[11]Miao, J. M. and Ho, M. H., "Effect of flexure on aerodynamic propulsive efficiency of flapping flexible airfoil," *J. Fluids Struct.*, Vol. 22, 2006, pp. 401–419.

[12]Dong, H., Mittal, R., and Najjar, F., "Wake topology and hydrodynamic performance of low aspect-ratio flapping foils," *J. Fluid Mech.*, Vol. 566, 2006, pp. 309–343.

[13]Ishihara, D., Horie, T., and Denda, M., "A two-dimensional computational study on the fluid-structure interaction cause of wing pitch changes in dipteran flapping flight," *J. Exp. Biol.*, Vol. 212, 2009, pp. 1–10.

[14]Ishihara, D., Yamashita, Y., Horie, T., Yoshida, S., and Niho, T., "Passive maintenance of high angle of attack and its lift generation during flapping translation in crane fly wing," *J. Exp. Biol.*, Vol. 212, 2009, pp. 3882–3891.

[15]Yang, T., Wei, M., and Zhao, H., "Numerical study of flexible flapping wing propulsion," *AIAA J.*, Vol. 48, No. 12, 2010.

[16]Zhao, H., Freund, J. B., and Moser, R. D., "A fixed-mesh method for incompressible flow-structure systems with finite solid deformations," *J. Comput. Phys.*, Vol. 227, 2008, pp. 3114–3140.

[17]Mohd-Yusof, J., "Combined immersed-boundary/B-spline methods for simulations of flow in complex geometries," Center for Turbulence Research, Annual Research Briefs – 1997, 1997.

[18]Brown, D. L., Cortez, R., and Minion, M. L., "Accurate projection methods for the incompressible Navier-Stokes equations," *J. Comput. Phys.*, Vol. 168, 2001, pp. 464–499.

[19]Kang, B. and Tan, C. A., "Parametric instability of a leipholz column under periodic excitation," *J. Sound Vib.*, Vol. 229, 2000, pp. 1097–1113.